Niobium-doped TiO$_2$ solid acid catalysts: Strengthened interfacial polarization, amplified microwave heating and enhanced energy efficiency of hydroxymethylfurfural production

Tuo Ji[a], Zheng Li[b], Chang Liu[b], Xiaohua Lu[b,*], Licheng Li[c], Jiahua Zhu[a,*]

[a] Intelligent Composites Laboratory, Department of Chemical and Biomolecular Engineering, The University of Akron, Akron, OH, 44325 USA
[b] State Key Laboratory of Material-Oriented Chemical Engineering, College of Chemistry and Chemical Engineering Department, Nanjing Tech University, Nanjing, 210009, PR China
[c] College of Chemical Engineering, Nanjing Forestry University, Nanjing, 210037, PR China

A R T I C L E   I N F O

A B S T R A C T

TiO$_2$ solid acid catalysts with different niobium (Nb) doping ratios (8, 16, and 24 mol%) were synthesized for microwave-assisted catalytic conversion of fructose to hydroxymethylfurfural (HMF). Nb doping has been demonstrated effective to enhance the quantity of acid sites and increase the acid strength. At optimal Nb loading of 16 mol%, it was found that the reaction rate constant and energy efficiency were significantly enhanced by 32 and 49%, respectively. The enhancement mechanism of Nb-doping was investigated by both experiment and density functional theory (DFT) calculation. It was revealed that Nb doping promoted the electron transfer from the bulk catalyst to surface sulfonic groups, resulting in enhanced acidity and polarity of sulfonic groups. The electron transfer could strengthen the sulfonic group-water interaction at catalyst surface and created a unique polarized interface region where heat generation and the catalytic reaction can be coupled for enhanced energy efficiency of such reactions.

1. Introduction

The increasing demand for sustainable energy and green chemical products has aroused significant interests in the development of advanced biomass conversion technologies [1–3]. Over 10-billion-ton biomass can be produced every year globally, while the existing challenges in the collection, processing, and conversion make the utilization rate extremely low [4,5]. Particularly, the complex biomass conversion met great challenges to develop a highly efficient and economically feasible process that directly transforms biomass into fuels [6,7]. It is therefore always appealing to develop an alternative process that converts biomass into valuable chemicals. Carbohydrate which represents the largest component of biomass is predominantly comprised of hexoses and pentoses and is widely found in almost all the biomass species [8,9]. Acid-catalyzed dehydration of hexoses and pentoses is demanding reaction due to the huge market potential of the resulting 5-hydroxymethylfurfural (HMF) and furfural products as they are key intermediates in future biorefineries [10,11]. Even though scale-up production of HMF has been commercialized (100–1000 KTA, kilometric ton per annum), the high temperature (150–200 °C) with

extended reaction time (1–6 hours) consume a huge amount of energy and make it impossible to reach the envisaged price of < \$2.5/kg [12].

In this scenario, existing studies are majorly devoted to developing new catalysts or new processes to shorten the reaction time and reduce manufacturing cost [13,14]. Microwave is one of the most promising technologies and has been successfully used to improve the reaction efficiency [15]. Microwave applies volumetric heating, which avoids the formation of heating gradient and thus uniform temperature field can be achieved [16]. The presence of "hot spots" where the temperature is higher than surrounding environment, has been demonstrated beneficial to improve reaction efficiency [17]. For example, Gronnow et al. systematically compared the energy efficiency of reactions with conventional oil bath heating and microwave heating at laboratory scale. They concluded that 85-fold energy reduction can be achieved for a Suzuki reaction under microwave heating [18]. Besides, the selection of proper catalyst is crucial to achieve the desired conversion. Recently, solid-acid catalysts are becoming more popular than conventional acid catalyst, mainly due to its lower corrosivity to reactors [19–21]. In heterogeneous reactions, heat needs to be transferred from heat source to catalyst surface and then can be utilized for

---

* Corresponding authors.
  E-mail addresses: xhlu@njtech.edu.cn (X. Lu), jzhu1@uakron.edu (J. Zhu).

reactions. In such a process, significant amount of heat was wasted to heat the liquid media and only a small fraction was used for reactions [22]. Moreover, most of the existing catalysts (e.g. SiO_2, ion-exchange resin and Amberlyst-15) are microwave-transparent which means they have no contribution to heat up the reaction in microwave [23,24]. In general, polar solvents are used to serve as heating media in microwave-heating reactions, but it poses a great barrier to apply microwave technology in non-polar solvent systems. Therefore, designing a new family of microwave-responsive catalyst could be more meaningful to be used in both polar and non-polar systems.

Titanium dioxide (TiO_2) has been used as solid acid catalyst in different reactions taking advantage of both Brønsted and Lewis acidic sites [25,26]. Though TiO_2 is microwave-transparent material, it can be engineered to enable microwave absorption by surface modification or crystal defect manipulation [27–29]. For example, Xia et al. found that TiO_2 nanocrystals can respond to electromagnetic wave at $2 \sim 18$ GHz due to the formation of an amorphous TiO_2 layer on the surface after surface hydrogenation [29]. The crystal defects at crystalline/amorphous interface play an important role that triggers microwave absorption at the grain boundary. Besides, our previous work demonstrated that $Ti-O-SO_4^{2-}$ acid sites were capable of polarizing the interlayer of protonated titanates ($H_2Ti_nO_{2n+1}$, n = 3, 5), which turned titanate into the microwave-responsive material and expedited the reaction rate of saccharide conversion reaction [22]. The $Ti-O-SO_4^{2-}$ not only serves as catalytic active sites, but also the site for heat generation under microwave irradiation. These unique features had led to a dramatic enhancement of reaction energy efficiency.

The surface structure and properties can be further promoted by incorporating n-type dopants, such as vanadium-(V), niobium (Nb), and tantalum (Ta) [30–32]. Nb is often preferred since Nb^{5+} (r = 0.70 Å) has a similar ionic radius as Ti^{4+} (r = 0.68 Å), and thus lattice mismatch between TiO_2 and Nb_2O_5 can be neglected. The electronic structure change by doping Nb in TiO_2 has been extensively discussed in previous literature [33–35]. Moreover, the multivalent cation doping also increases the electrical conductivity of TiO_2. Therefore, it is expected that Nb-doping in sulfonated TiO_2 solid catalyst would change the surface polarization of sulfonic acid groups and further affect its microwave absorption as well as catalytic properties.

In this work, sulfated Nb-doped TiO_2 was synthesized via co-sintering method and was employed as microwave responsive catalysts for biomass conversion reactions. Effect of Nb doping on the TiO_2 structure and surface acid properties were investigated via both experiment and density functional theory (DFT) calculations. The catalytic activity and energy efficiency of titanate catalysts were studied in fructose to HMF conversion reactions at different microwave power levels. Combined with the structural and physicochemical features of Nb-doped TiO_2, the mechanism of microwave absorption and related Nb-doping effect on reaction efficiency were proposed and systematically studied.

2. Experimental

2.1. Materials

Potassium carbonate (K_2CO_3, $\geq 99.0\%$), titania (TiO_2 nanopowder, > 99.5%), niobium (V) oxide (Nb_2O_5, 99.99%) and D-(-)-fructose ($C_6H_{12}O_6$ $\geq 99\%$), were purchased from Sigma-Aldrich. Sulfuric acid (H_2SO_4, 98.0%) was purchased from Fisher Scientific. All reagents were used as received without further purification. Deionized water was purified using a Milli-Q direct-8 ultrapure water system (Millipore, Billerica, MA) with a minimum resistivity of 18.2 MΩ cm and used for all experiments.

2.2. Preparation of Nb-doped TiO_2

Nb-doped TiO_2 was prepared by a co-sintering method. Nb_2O_5, TiO_2, and K_2CO_3 were firstly mixed at different ratios according to the

doping level of Nb. 50 mmol TiO_2 and 80 mmol K_2CO_3 were used as base and Nb_2O_5 was added in the base at 5, 10, and 15 mmol to control the Nb doping levels of 8, 16 and 24 mol%, respectively. These components were mixed thoroughly and then pressed tightly in the corundum crucibles. The crucibles were then placed in a tube furnace and heated up to 870 °C ($\pm$ 10 °C) with a ramping rate of 5 °C/min. The temperature was kept at 870 °C for 4 h, Fig. S1. A hydration process was then applied to generate mesopores in Nb-doped K_2TiO_3. Specifically, the crucibles with solid products were placed in a sealed chamber (4 L) together with 100 mL H_2O at the bottom of the chamber, Fig. S2. This process took 24 h, and the solid products became softer by the absorbed moisture. After that, the hydrated Nb-doped K_2TiO_3 was rinsed by 0.1 M H_2SO_4 aqueous solution for 4 times, where K ions in the crystal skeleton are gradually replaced by H ions and SO_4^{2-} ions remained at solid surface. The resulting samples were dried and then heated at 400 °C for 2 h to form sulphonic groups on TiO_2 surface. The products with different Nb ratios were named TiNb8, TiNb16, and TiNb24, respectively. The control sample without Nb was named TiNb0.

2.3. Characterizations

The powder X-ray diffraction analysis was carried out with a Bruker AXS D8 Discover diffractometer with GADDS (General Area Detector Diffraction System) operating with a Cu-K α radiation source filtered with a graphite monochromator (λ = 1.541 Å). A TriStar II 3020 surface analyzer (Micromeritics Instrument Corp., USA) was employed to analyze the structural properties. The Brunauer–Emmett–Teller (BET) surface area of materials was calculated by N_2 adsorption-desorption isotherms at 77 K. The pore size distribution was calculated by the Barrett-Joyner-Halenda (BJH) method from the adsorption branch. Morphology evolution of Nb-doped TiO_2 was characterized by scanning electron microscopy (SEM, JEOL-7401) and transmission electron microscopy (FEI Scanning TEM). EDAX energy dispersive X-ray spectrometer was used to quantify the surface element composition. Ammonia temperature programmed desorption (NH_3-TPD) was carried out to analyze the acidity of catalysts. In detail, 100 mg catalyst was loaded into a U-shaped tube glass cell and flushed with helium at 450 °C for 2 h. After cooling to 150 °C, the system was purged with NH_3 for 30 min at a flow rate of 20 mL/min. After that, helium gas was purged for 30 min to flush out the excess NH_3. The NH_3 desorption was carried out in the temperature range of 150–600 °C with a heating rate of 10 °C/min. The amount of desorbed NH_3 was continuously monitored within the temperature range. Fourier transform infrared (FTIR) spectra were recorded with a Digilab Excalibur FTS 3000 series FT-IR Spectrometer using KBr pellets, and the thickness of the pellet is about 1 mm. X-ray photoelectron spectroscopy (XPS) was carried out using a PHI VersaProbe II Scanning XPS Microprobe with Al-K α line excitation source. To test the electromagnetic properties of Nb-doped composites, they were mixed with paraffin (50:50 wt) wax and then pressed into cylindrically shaped compacts (inner diameter 3.04 mm, outer diameter 7.00 mm). The complex permeability and permittivity of the compacts were recorded in the frequency range of 2.0–12.0 GHz with an Agilent N5230 A network analyzer.

2.4. Catalytic reaction under microwave irradiation

Fructose dehydration reaction was carried out in a tube (10 mL, ID = 12 mm) reactor under microwave irradiation. Firstly, 0.55 mmol fructose and 50 mg catalyst were added into 4.0 mL water and then sonicated for 5 min. The mixture was then transferred to the tube reactor, which was placed in a microwave reactor (Discover SP, CEM). The system temperature was measured by IR temperature sensor outside the bottom of the reaction vessel. The reaction proceeded at different power levels for a given reaction time. After that, system temperature was cooled down to room temperature. The resulting solution was then filtered with a syringe filter (VWR, 0.22 mm PTFE). Two

programming modes were adopted to test the performance of the catalysts. Temperature-control mode was used to study the intrinsic catalytic activity, where the temperature was set at 130–150 °C and maximum pressure was controlled under 300 psi. The power-control mode was used to study the capability of heat generation among the synthesized catalysts. The input power of microwave was adjusted between 13–19 W and maximum pressure was controlled under 300 psi. The filtrate was then analyzed by both UV–vis spectrophotometry and HPLC equipped with RI detector and HPX-87 column with 0.17 mL/min of distilled water at 55 °C. The calculation of fructose conversion and HMF yield was detailed in our previous paper [21].

2.5. Computational details

All the calculations were carried out using Material Studio modeling DMol³. The exchange and correlation interaction were modeled using Perdew–Purke–Ernzerhof (PBE) function with generalized gradient approximation (GGA). Anatase TiO_2 (101) supercell layer structure was selected since it's the main exposed surface [36,37]. Two sulfonic groups (SO_4^{2-}) and two hydroxyl groups were grafted on Ti_{4C}. The Nb doping was performed by replacing four Ti lattice atoms by Nb atoms. A periodic boundary condition was adopted to model this slab, and the area of the surface was 10.886×7.552 Å having 62 atoms. The vacuum region was set to 1.0 nm in order to avoid the interference. The Brillouin zone of the Monkhorst − Pack grid was set at $3 \times 3 \times 1$. The self-consistent field (SCF) energy was set to 2×10^{-6} eV/atom and the value of smearing was set to be 0.1 eV. Spin polarization was also applied, and the real space cutoff radius was maintained at 3.0 Å.

3. Results and discussion

3.1. Micro-structure characterization

Fig. 1 shows the XRD spectra of TiO_2 and Nb-doped TiO_2 with different Nb doping ratios. The peaks at 25.3, 36.9, 37.9, 48.1, 53.8, 55.3 and 62.7° are signature features of anatase TiO_2 (JCPDS #21-1272). With the increase of Nb ratio, the main peak at 25.3° shifted to lower 2θ angle, inset of Fig. 1, which can be attributed to the expanded lattice spacing due to the insertion of Nb^{5+} (0.64 Å) into TiO_2 lattice of Ti^{4+} (0.61 Å). At lower Nb doping ratios of 8 and 16 mol%, Nb existed in the form of mixed oxide $Ti_2Nb_{10}O_{29}$ (JCPDS #13-0316) and Nb_2O_5 was not observed, Fig. S3. With increasing Nb ratio to 24 mol%, new peaks at 22.3 and 27.3° appeared, indicating the formation of potassium niobate ($KNbO_3$). $KNbO_3$ was formed by the reaction between Nb_2O_5 and
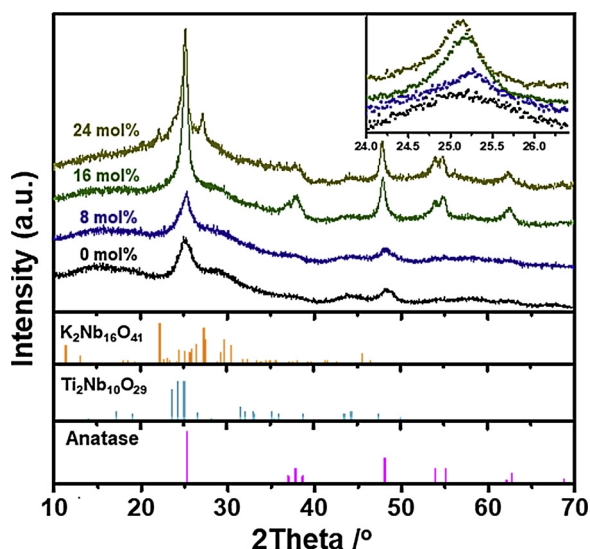
K_2CO_3 (Fig. S4, JCPDS #32-0822) only when Nb_2O_5 was in excess amount during calcination. Overall, the introduction of Nb promoted the formation of TiO_2 crystal phase. The intensity of anatase (TiO_2) peaks was enhanced after incorporating Nb_2O_5 and the peak intensity became stronger. The gradual increase of crystal size was also observed at 6.5, 7.0, 11.8, and 13.0 nm by increasing Nb doping ratio (0, 8, 16 and 24 mol%, respectively).

Both TEM and SEM were used to study the morphology evolution of TiO_2 with the increase of Nb doping ratio. As shown in Fig. 2(a), TiNb0 shows a loose structure with obvious stacking pores. The formation of porous structure could be attributed to the structural collapse of potassium titanate during the hydration process [38]. Increasing Nb ratio gradually decreased porosity and turned the loose structure into solid, Fig. 2(b–d). Such structural transition from loose to solid was also observed by SEM, Fig. 2(e–h).

To better understand the TiO_2 structural evolution with the addition of Nb element, nitrogen adsorption-desorption isotherms were performed. All the materials showed type IV isotherm pattern with hysteresis loop, indicating the presence of mesoporous structure, Fig. 3(a). After analyzing the adsorption branch of TiNb0, two different pore sizes at 4.0 and 14.2 nm were obtained, Fig. 3(b). Such binary mesopore distribution disappeared after incorporating Nb element. Increasing Nb ratio resulted in a decreased of surface area in general which was consistent with the observed structural transition from porous to solid. Detailed structural characterization results are summarized in Table 1. The surface area increased from 66 to 81 $m^2 g^{-1}$ after doping 8 mol% Nb in TiO_2, which then dramatically reduced to 17 and 2.3 $m^2 g^{-1}$ after further increasing Nb loading to 16 and 24 mol%, respectively.

3.2. Investigation of surface properties

FT-IR absorption bands observed at 540 and 460 cm^{-1} were assigned to the vibration of the Ti-O bond, Fig. 4. The appearance of a broad peak at ~610 cm^{-1} is from the Nb-O stretching vibration. The peaks at 1633 and 3404 cm^{-1} are associated with the bending and stretching vibrations of hydroxyl groups. These hydroxyl groups could be attributed to the disassociated water molecules or exposed OH groups on the TiO_2 surface [39]. Besides the characteristic peaks of Nb/TiO_2, the absorption within the range of 900-1400 cm^{-1} implied the existence of SO_4^{2-} groups on the surface. Specifically, the peaks at about 1216, 1125, and 1044 cm^{-1} can be attributed to v_3 vibrations of bidentate SO_4^{2-} in a C_{2v} symmetry while the band at 990 cm^{-1} can be assigned to the v_1 vibration. Among them, peaks at 1044 and 990 cm^{-1} corresponds to the asymmetric and symmetric S−O stretching vibrations respectively [40]. The other two peaks at 1216 and 1125 cm^{-1} were associated with the asymmetric and symmetric stretching of S=O vibrations. The major change occurred at the peak position of 1383 cm^{-1}, where a gradual decrease was observed with increasing Nb ratio. This peak can be ascribed to the S=O stretching vibration from sulfonic ion (HSO_4^-) or SO_3 with weak chemical or physical absorption on the solid surface [41]. The gradual decrease of this peak revealed that Nb-doping was beneficial to strengthen the bonding of sulfonic groups on the solid surface. Energy dispersive spectrum was conducted to quantify the sulfonic acid on the surface, Fig. 5. Table 1 summarized the atomic percentage of Ti, Nb, O, and S elements. A gradual increase of S element was observed in TiNb0 (3.01 at%), TiNb8 (3.51 at%), TiNb16 (5.06 at %) and TiNb24 (5.68 at%), revealing the fact that larger grafting density of surface SO_4^{2-} groups can be achieved at higher Nb doping ratio. Potassium element was not detected from both EDX (Fig. 5) and XPS analysis (Fig. S5), implying that potassium was completely removed during the ion-exchange process.

NH_3-TPD was used to analyze the interaction between sulfonic groups and TiO_2 surface, Fig. 6. The amount of desorbed NH_3 allowed a quantitative assessment of surface sulfonic groups, whereas the desorption temperature was an indicator of the acid strength. For general solid-acid catalysts, the desorption peaks at < 200, 200–400, and

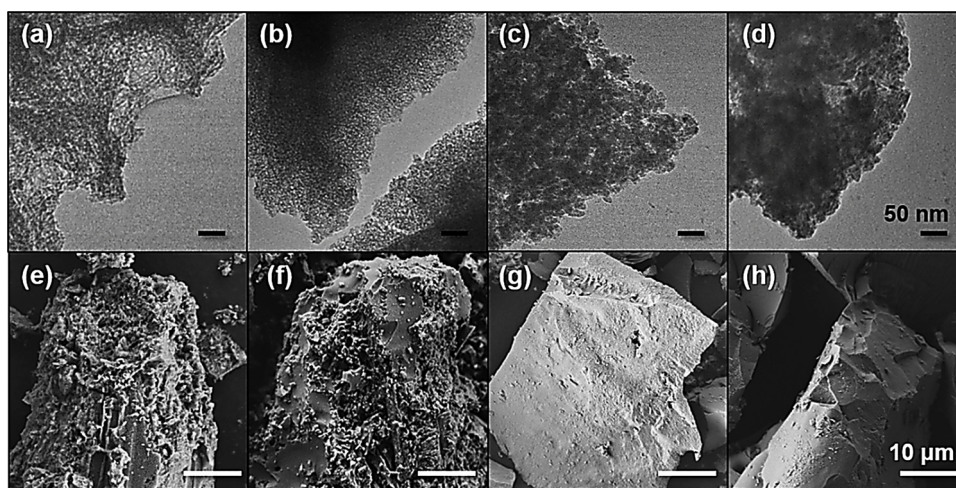**Fig. 1.** XRD spectra of Nb-doped TiO_2 with different Nb ratios.

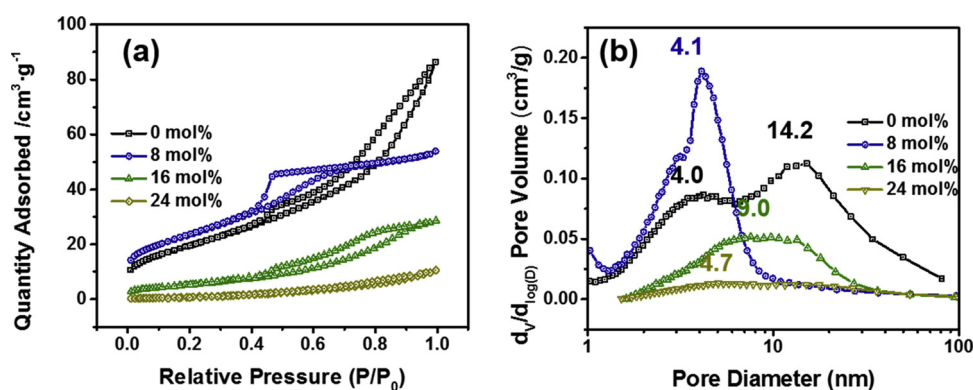Fig. 2. TEM and SEM images of (a&e) TiNb0, (b&f) TiNb8, (c&g) TiNb16, and (d&h) TiNb24.

Fig. 3. (a) Nitrogen adsorption-desorption isothermal and (b) pore size distribution of Nb-doped TiO_2 with different doping ratios.

400–600 °C temperature regions represented weak, medium-strong and strong acid sites, respectively [42,43]. The TiNb0 showed two desorption peaks centered at 124 and 512 °C, which can be assigned to the physical absorbed and chemically bonded sulfonic groups on the TiO_2 surface. A broad peak from 200 to 400 °C indicated that part of the sulfonic groups was weakly bonded to the solid surface. After doping 8 mol% Nb, the NH_3 desorption below 200 °C was greatly suppressed and a new board peak was formed at the peak position of 367 °C. Meanwhile, the peak position in 400–600 °C range slightly shifted from 512 to 518 °C, indicating an enhanced acid strength after Nb doping. Further increasing Nb ratio to 16 mol%, NH_3 desorption below 400 °C becomes negligible, which all shifted to the high-temperature range with the peak position at 519 °C. In other words, the strong acid sites became dominant in the TiNb16 catalyst. Such enhancement of acid strength was consistent with the bond evolution as evidenced by the FT-IR results. Similar desorption peak was not obvious in TiNb24 within the defined temperature range, indicating the low quantity of acid groups on the surface. Even though a large fraction of the sulfur

element was detected by EDX as summarized in Table 1, the low surface area of TiNb24 restricted the up-taking of acid groups in large quantity.

3.3. Intrinsic activity studies

The intrinsic catalytic activity of TiO_2 and Nb-doped TiO_2 was compared in the fructose conversion reaction, Fig. 7. With controlled reaction temperature at 150 °C, HMF yield in 2 min could reach 27.0, 31.8, 40.5, and 18.9 mol% by using TiNb0, TiNb08, TiNb16, and TiNb24, respectively. The HMF yield in such a short time is significantly higher than other solid acid catalysts as reported in previous literature [44–47]. When the reaction proceeded to 4 min, the HMF yield reached the highest and side reaction began due to the non-selective dehydration of fructose. The reaction rate of fructose conversion was calculated by pseudo-first order model, which was based on the assumptions that HMF was stable enough and side reaction was negligible. With that, the reaction rate of fructose ($r_{fructose}$) can be calculated by Eq. (1):

Table 1
Characteristics of Nb-doped TiO_2 materials.

Entry	Nb ratio /mol%	Structure information				Surface element (At%)		
		SA(m^2/g)	V_p(cm^3/g)	D_p(nm)	D_c(nm)	Ti	Nb	S
TiNb0	0	66	0.10	5.3	6.5	14.47	0	3.01
TiNb8	8	81	0.07	3.7	7.0	13.25	1.33	3.51
TiNb16	16	17	0.03	6.3	11.8	11.74	3.12	5.06
TiNb24	24	2.3	0.01	5.6	13.0	07.26	4.03	5.68

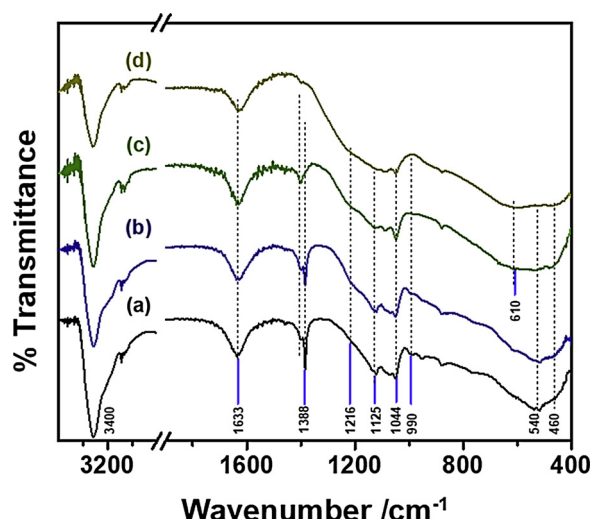SA: surface area, V_p: pore volume, D_p: pore size, D_c: crystal size.

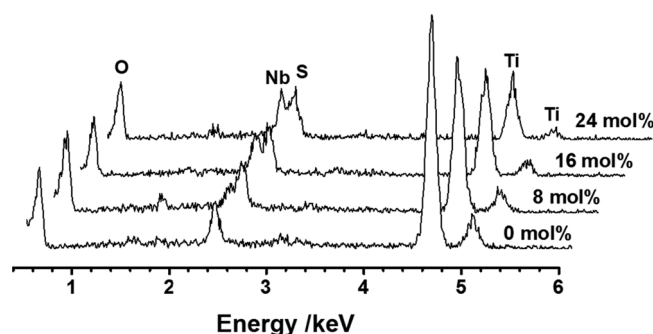**Fig. 4.** FT-IR spectra of (a) TiNb0, (b) TiNb8, (c) TiNb16, and (d) TiNb24.

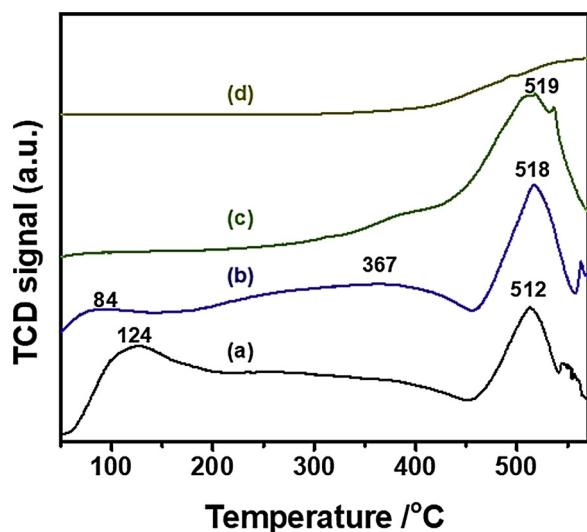**Fig. 5.** EDX spectra of Nb-doped TiO$_2$ with different Nb doping ratios.

Fig. 6. NH$_3$-TPD of (a) TiNb0, (b) TiNb8, (c) TiNb16, and (d) TiNb24.

$$r_{fructose} = \frac{d(ln(C_t/C_0))}{dt} = -k \tag{1}$$

where C_0 is the initial fructose concentration, C_t is the fructose concentration at time t, k is the rate constant of fructose dehydration at a certain temperature. Keeping all the reaction parameters the same, the k value reflected the intrinsic catalytic activity of the four catalysts. With linear fitting of $ln(C_t/C_0)$ versus t, it was suggested that the kinetic data agreed well with the pseudo-first order reaction model, Fig. 7(b).

The rate constant k increased from 0.44 to 0.46 and 0.58 min^{-1} with Nb doping of 8 and 16 mol% respectively while it dropped down to 0.24 min^{-1} in TiNb24. Providing the strongest acidity among the catalysts, TiNb16 exhibited the highest HMF yield and fastest reaction rate. The activation energy of the reaction by using the four catalysts was calculated as well, which is detailed in Fig. S6. Activation energy is an empirical value that represents the energy required to overcome the energy barrier for the chemical reaction. All the catalysts showed the similar value of 150 kJ·mol^{-1}, suggesting a similar surface-controlled reaction route where the reaction rate was determined by the quantity of acid sites on the catalyst surface.

3.4. Microwave absorption studies

Not only system temperature affects the reaction efficiency, the heat generation capability of the developed catalysts also influences the micro-environment at catalyst surface and thus potentially drives the surface reaction in a different way. The temperature profile of each reaction was monitored at a fixed microwave power of 15 W, Fig. 8(a). The temperature of the reaction solution rapidly climbed up in the first 5 min and then gradually slowed down to reach equilibrium plateau. The difference in equilibrium temperature (T_e) was attributed to the varied heat-generation capability of the catalysts. In general, a catalyst with better microwave absorption would lead to higher system temperature. The inset of Fig. 8(a) summarized the change of T_e as a function of Nb doping ratio. T_e raised from 146 to 161 °C with increasing Nb ratio to 16 mol% and then dropped to 151 °C at 24 mol% Nb, which was highly consistent with the variation of reaction rate observed from the intrinsic activity study. The higher reaction temperature is often favored to expedite reaction rate while it also drives side reaction due to the endothermic nature of fructose dehydration reaction [48]. Among the four catalysts, TiNb16 showed the highest HMF yield (56 mol%) and fructose conversion (97 mol%) within 20 min, Fig. 8(b). Although TiNb0 and TiNb8 have the similar reaction rate constant at 150 °C, higher yield and conversion were observed with TiNb8 probably due to its better microwave heating capability. More details will be discussed in following section of mechanism study.

The communication between catalyst and microwave determines the temperature field surrounding the catalyst and thus the reaction. In this work, the intensity of input energy has been adjusted by tuning the input power level of microwave and its impact on reaction efficiency was investigated, Fig. 8(c). In general, larger input power generates higher system temperature. By increasing input power from 13 to 19 W, the system temperature went up from 131 to 166 °C with TiNb16 catalyst (10 min reaction), which is the most significant among the catalysts.

To quantitatively compare the energy efficiency of the reaction, efficiency coefficient was introduced that can be calculated from Eq. (2)

$$Efficiency\ coefficient\ j = \frac{[HMF]}{P \cdot t \cdot V} \tag{2}$$

where j is the efficiency coefficient in mmol·(KJ·L)$^{-1}$, P is the input power of microwave, t is elapsed time, V is the volume of the reaction solution. The efficiency coefficient reflects the overall performance of the catalyst in terms of the intrinsic activity and the microwave heating capability. The efficiency coefficient at different power levels was summarized in Fig. 8(d). The energy efficiency coefficient of all catalysts gradually increased with increasing power level from 13 to 19 W, Fig. 8(d). TiNb16 reached the highest coefficient of 6.7 mmol·(KJ·L)$^{-1}$ at 19 W, which was attributed to its largest number of Brønsted acid sites and excellent microwave absorption ability.

3.5. Mechanism of catalyst & microwave interaction

To better understand how microwave drives higher reaction efficiency, it is critically important to know the interaction of microwave
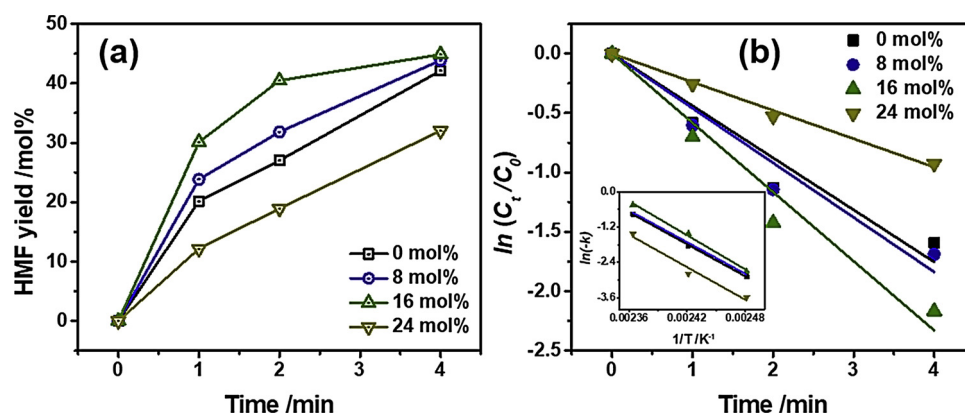
Fig. 7. (a) HMF yields versus time, (b) $ln(C_t/C_0)$ versus reaction time of fructose dehydration. Inset figure is Arrhenius plots. Reaction condition: [fructose] = 0.55 mmol, [catalysts] = 12.5 mg/mL, temperature = 150 °C.
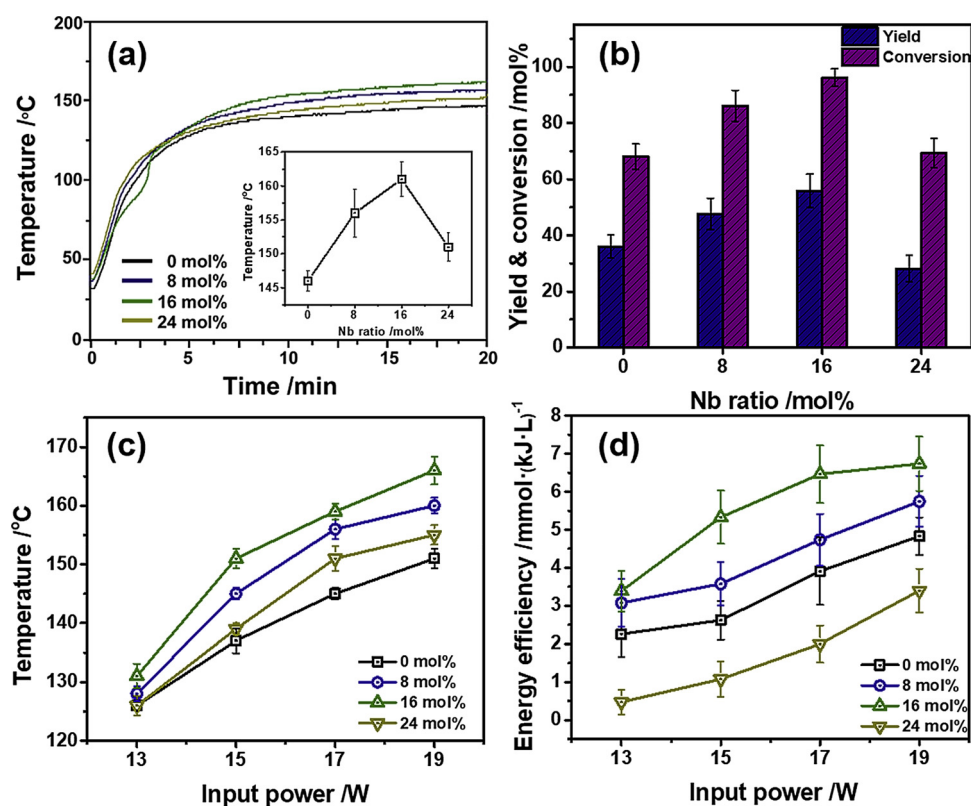

Fig. 8. (a) System temperature profile, (b) HMF yield and fructose conversion as a function of Nb doping ratio. Reaction condition: [fructose] = 0.55 mmol, [catalysts] = 12.5 mg/mL, input power = 15 W. Time = 20 min (c) Equilibrium temperature vs. input power and (d) Energy efficiency vs. input power at 20 min.

with the bulk catalyst as well as the catalyst surface where the reaction occurs. The complex permittivity ($\varepsilon = \varepsilon' + i\,\varepsilon''$) and permeability ($\mu = \mu' + i\,\mu''$) of solid catalysts were characterized to understand the microwave absorption property of bulk catalyst. The real parts ε' and μ' are related to the stored electrical and magnetic energy; the imaginary parts ε'' and μ'' are associated with the dissipation (or loss) of electrical and magnetic energy. The conversion of microwave energy to heat can be calculated by Eq. (3) [49].

$$Q = 2\pi\varepsilon_0\varepsilon''fE^2 \tag{3}$$

where Q is generated heat (W/m^3), f is the frequency of the energy source (Hz), ε_0 is the permittivity of vacuum or free space (8.85 × 10^{12} F/m). A larger dielectric loss (ε'') is beneficial for heat generation in the system. The dielectric constant of TiNb0 was relatively larger (ε' = 4.7–5.0) compared to other Nb-doped TiO$_2$ (< 4.2), Fig. 9(a). It

was worth noting that all the catalysts showed a much smaller dielectric loss (< 0.3) comparing to microwave absorbers. [50,51] In other words, these catalysts were not good microwave absorbers and Nb doping did not help to facilitate microwave absorption. The reduced ε' and ε'' in Nb doped TiO$_2$ suggested a weakened catalyst/microwave interaction in the solid state.

Revealing the interaction between microwave and catalyst surface could help to understand the fundamental role of the microwave in the reaction. As demonstrated earlier, the reaction followed a surface reaction route where the reaction rate was influenced by the available reactive sites on the catalyst surface. The sulfonic groups on catalyst surface could be responsible for the reaction in this case. In this work, a control experiment was designed to verify the role of surface sulfonic groups in microwave heating. Specifically, another set of catalysts were prepared in which the sulfonic groups were eliminated. Briefly, SO$_4$$^{2-}$
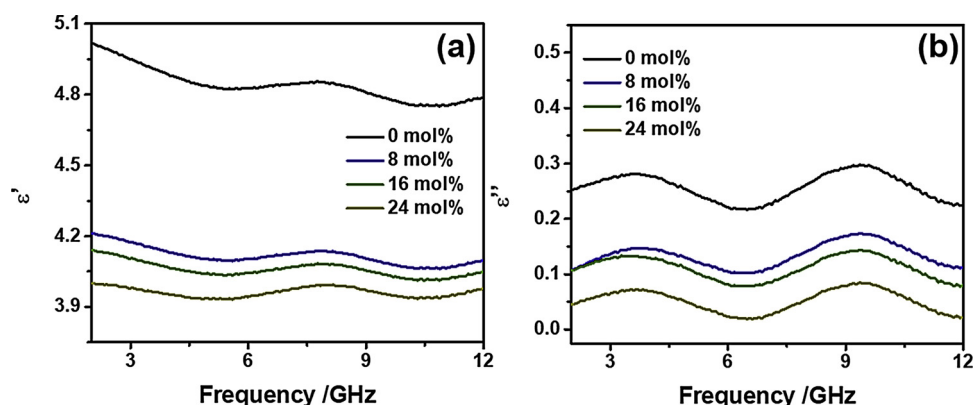
Fig. 9. (a)Real part (ε') and (b) imaginary part (ε'') of the permittivity of TiO_2 and Nb-doped TiO_2.
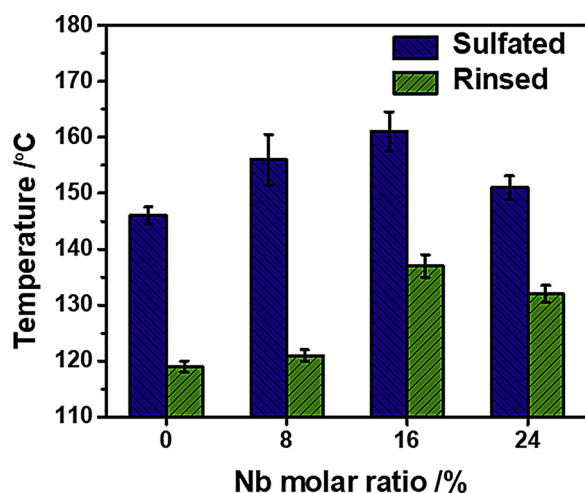

Fig. 10. System temperature by using sulfated and rinsed Nb-doped TiO_2 as catalysts under 15 W microwave irradiation. Reaction condition: [fructose] = 0.55 mmol, [catalysts] = 12.5 mg/mL, volume = 4 mL.

Fig. 11. High-resolution XPS peak of Ti2p for TiNb0 and TiNb16.

residues were removed after ion-exchange process by rinsing thoroughly with ammonia water and then the desulphonated titanates were heated at 400 °C. The microwave heating was then performed with these materials at 15 W and the system temperature was summarized in Fig. 10. It was obvious that the elimination of sulfonic groups led to a dramatic drop of system temperature in all samples. For example, the system temperature with pure TiO_2(TiNb0) decreased from 146 to 119 °C, which is very close to a blank fructose solution. A similar phenomenon was observed in TiNb8. The rinsed TiNb16 and TiNb24 showed obvious higher temperature than TiNb0 and TiNb8, even though the system temperature was also significantly dropped. Therefore, the sulphonic groups are critical to the microwave heating capability of the catalysts. It showed that sulfur element was thoroughly removed in TiNb0 while slight amount remained in TiNb8, Fig. S7. 3.24 and 2.87 at% sulfur still remained in TiNb16 and TiNb24 after rinsing. The presence of sulphonic groups suggested that Nb-doping strengthen the acid sites.

The effect of Nb-doping on the strength of sulfonic groups could be explained by the electron transfer mechanism. Once high-valence Nb (V) was doped in the TiO_2, more electrons could be drawn from the bulk to the surface. Fig. 11 compared the XPS peaks of Ti2p from TiNb0 and TiNb16. Compared to TiNb0, Ti2p peak of TiNb16 shifted to higher binding energy, suggesting an electron redistribution process with more concentrated electrons surrounding Nb atom. These electrons tend to transfer to sulfonic groups on the surface, and thus enhanced the acid strength. It can be concluded that Nb-doping had a negligible impact on the intrinsic microwave properties however such doping has led to the increase of the quantity of acid sites in addition to improved acid strength.
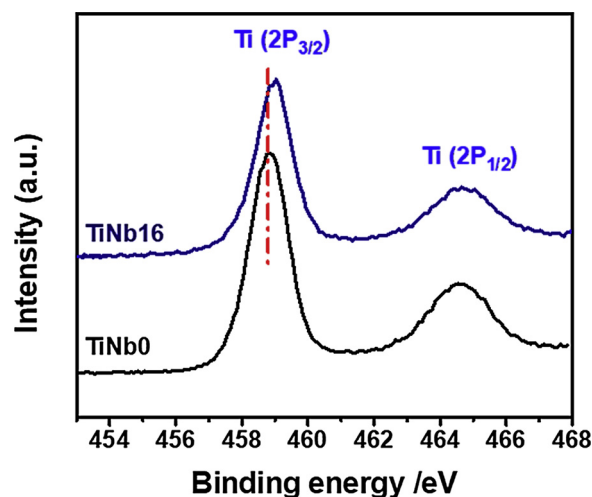
To confirm the electron transfer mechanism, two models of TiO_2/SO_4^{2-} and Nb-doped TiO_2/SO_4^{2-} were established and analyzed by DFT calculation. The detailed information about the models was illustrated in Section 2.5. As shown in Fig. 12, Nb atoms replaced the Ti in the crystal structure and connected with 5 oxygen atoms. After geometry optimization, the averaged Mulliken bond lengths and charge population of sulfonic groups of the two models are provided in Table 2. The Nb atoms showed larger positive charge (1.595) than Ti atoms (1.347). The charge of Ti slightly increased from 1.347 to 1.354 after doping Nb atoms in the TiO_2 skeleton. However, the charge of $O_{(S=O)}$ significantly decreased from -0.555 to -0.705. These results suggested a more negative surface formed once the Nb-doping. Such electron transfer not only enhanced the acidity of sulfonic groups, but also improved the interaction between sulfonic group and H_2O molecule. Meanwhile, the length of O-Ti_{5C} bond decreased from 2.283 to 2.050 Å, suggesting an enhanced interaction between sulfonic group and TiO_2 surface. These results were highly consistent with experimental observations.

4. Conclusions

To sum up, this work presented a systematic study on the preparation and characterization of a new type of microwave-responsive solid acid catalysts that showed excellent energy efficiency in fructose to HMF conversion reactions. TiO_2 was used as solid acids and Nb element was doped to optimize the structural and catalytic properties.
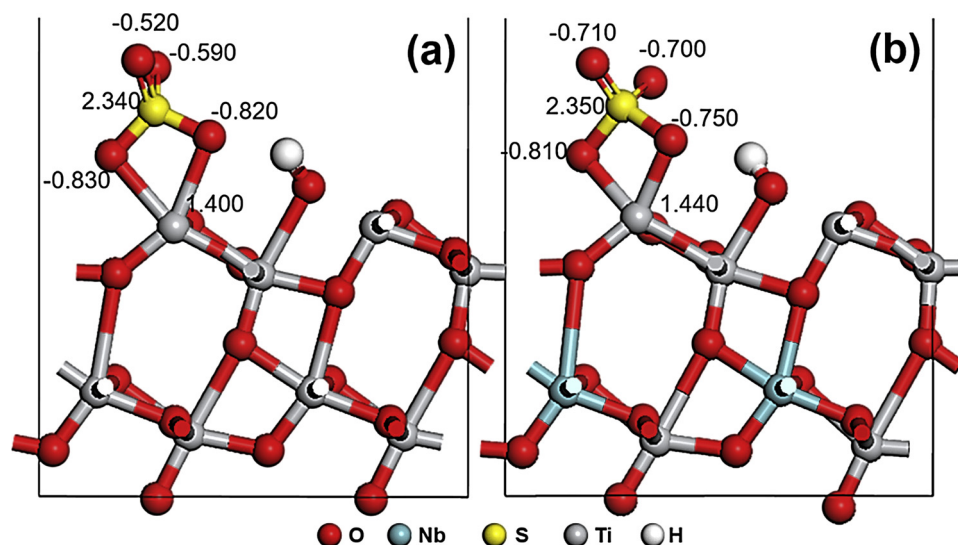
Fig. 12. Calculation models of sulfonic group grafted on (a) Anatase (101) and (b) Nb-doped Anatase (101) surface.

Table 2
The averaged bond length and Mulliken charge.

	TiO$_2$(101)-SO$_4{}^{2-}$	Nb-doped TiO$_2$(101)-SO$_4{}^{2-}$
l O = S	1.515	1.457
l O-S	1.484	1.550
l O-Ti$_{5c}$	2.283	2.050
q S	2.340	2.350
q O$_{(S=O)}$	−0.555	−0.705
q Ti	1.347	1.354
q O$_{(S-O)}$	−0.825	−0.780
q H	0.450	0.450
q Nb	–	1.595

Results indicated that the sulphonic groups are critical to the microwave heating capability of the catalysts; Nb doping was beneficial to increase the quantity of surface sulfonic groups as well as the acid strength. Therefore, an optimal Nb loading of 16 mol% (TiNb16) was found, which achieved the highest reaction rate constant of 0.58 min^{-1} and HMF yield of 40.5 mol%. Nb doping also increased the acid strength of sulfonic groups, which has been proved by both experiment and DFT calculations. XPS results confirmed an electron redistribution process in TiNb16, and DFT calculation further revealed electron transfer caused a more negative sulphonic group formed on the surface. Such electron transfer strengthened the sulfonic group-water molecule interaction and created a unique polarized interface at catalyst surface. Under microwave irradiation, the heat generation and catalytic conversion can be coupled at the interface and thus can greatly expedite the reaction rate. With such unique feature, the energy efficiency of the reaction can be enhanced by 49%. Overall, this work offers a new approach to couple the design of solid catalyst and its responsive behavior in the microwave. The improved energy efficiency by using such catalysts has great potential to enable the economic feasibility of biomass conversion reactions.

Acknowledgments

Appendix A. Supplementary data

Supplementary material related to this article can be found, in the online version, at doi:https://doi.org/10.1016/j.apcatb.2018.11.013.

References

[1] N. Panwar, S. Kaushik, S. Kothari, Role of renewable energy sources in environmental protection: a review, Renew Sustain Energy Rev 15 (2011) 1513–1524.
[2] D. Carpenter, T.L. Westover, S. Czernik, W. Jablonski, Biomass feedstocks for renewable fuel production: a review of the impacts of feedstock and pretreatment on the yield and product distribution of fast pyrolysis bio-oils and vapors, Green Chem 16 (2014) 384–406.
[3] S. Eibner, A. Margeriat, F. Broust, D. Laurenti, C. Geantet, A. Julbe, J. Blin, Catalytic deoxygenation of model compounds from flash pyrolysis of lignocellulosic biomass over activated charcoal-based catalysts, Appl Catal B 219 (2017) 517–525.
[4] H. Li, Z. Fang, J. Luo, S. Yang, Direct conversion of biomass components to the biofuel methyl levulinate catalyzed by acid-base bifunctional zirconia-zeolites, Appl Catal B 200 (2017) 182–191.
[5] R. Davda, J. Shabaker, G. Huber, R. Cortright, J.A. Dumesic, A review of catalytic issues and process conditions for renewable hydrogen and alkanes by aqueous-phase reforming of oxygenated hydrocarbons over supported metal catalysts, Appl Catal B 56 (2005) 171–186.
[6] P. McKendry, Energy production from biomass (part 1): overview of biomass, Bioresour Technol 83 (2002) 37–46.
[7] L. Zhang, Z. Liu, G. Cui, L. Chen, Biomass-derived materials for electrochemical energy storages, Prog Polym Sci 43 (2015) 136–164.
[8] A.J. Ragauskas, C.K. Williams, B.H. Davison, G. Britovsek, J. Cairney, C.A. Eckert, W.J. Frederick, J.P. Hallett, D.J. Leak, C.L. Liotta, The path forward for biofuels and biomaterials, Science 311 (2006) 484–489.
[9] R.M. Baldwin, K.A. Magrini-Bair, M.R. Nimlos, P. Pepiot, B.S. Donohoe, J.E. Hensley, S.D. Phillips, Current research on thermochemical conversion of biomass at the National Renewable Energy Laboratory, Appl Catal B 115 (2012) 320–329.
[10] J.J. Bozell, G.R. Petersen, Technology development for the production of biobased products from biorefinery carbohydrates-the US Department of Energy's "Top 10" revisited, Green Chem 12 (2010) 539–554.
[11] M. Yabushita, H. Kobayashi, A. Fukuoka, Catalytic transformation of cellulose into platform chemicals, Appl Catal B 145 (2014) 1–9.
[12] M. Bicker, J. Hirth, H. Vogel, Dehydration of fructose to 5-hydroxymethylfurfural in sub- and supercritical acetone, Green Chem 5 (2003) 280–284.
[13] L. Vilcocq, P.C. Castilho, F. Carvalheiro, L.C. Duarte, Hydrolysis of oligosaccharides over solid acid catalysts: a review, ChemSusChem 7 (2014) 1010–1019.
[14] F. Liu, K. Huang, A. Zheng, F.-S. Xiao, S. Dai, Hydrophobic solid acids and their catalytic applications in green and sustainable chemistry, ACS Catal 8 (2017) 372–391.
[15] H. Cho, C. Schäfer, B. Török, Microwave-assisted solid acid catalysis, Microwaves Catal Method Appl (2015) 5.
[16] C.O. Kappe, Controlled microwave heating in modern organic synthesis, Angew Chem Int Ed 43 (2004) 6250–6284.
[17] W. Xu, J. Zhou, Z. Su, Y. Ou, Z. You, Microwave catalytic effect: a new exact reason for microwave-driven heterogeneous gas-phase catalytic reactions, Catal Sci Technol 6 (2016) 698–702.
[18] M.J. Gronnow, R.J. White, J.H. Clark, D.J. Macquarrie, Energy efficiency in chemical reactions: a comparative study of different reaction techniques, Org Process

Res Dev 9 (2005) 516–518.

[19] X. Li, Y. Zhang, The conversion of 5-hydroxymethyl furfural (HMF) to maleic anhydride with vanadium-based heterogeneous catalysts, Green Chem 18 (2016) 643–647.

[20] Q. Hou, M. Zhen, L. Liu, Y. Chen, F. Huang, S. Zhang, W. Li, M. Ju, Tin phosphate as a heterogeneous catalyst for efficient dehydration of glucose into 5-hydroxymethylfurfural in ionic liquid, Appl Catal B 224 (2018) 183–193.

[21] T. Ji, R. Tu, L. Mu, X. Lu, J. Zhu, Structurally tuning microwave absorption of core/shell structured CNT/polyaniline catalysts for energy efficient saccharide-HMF conversion, Appl Catal B 220 (2018) 581–588.

[22] T. Ji, R. Tu, L. Li, L. Mu, C. Liu, X. Lu, J. Zhu, Localizing microwave heat by surface polarization of titanate nanostructures for enhanced catalytic reaction efficiency, Appl Catal B 227 (2018) 266–275.

[23] I. Bilecka, M. Niederberger, Microwave chemistry for inorganic nanomaterials synthesis, Nanoscale 2 (2010) 1358–1374.

[24] D.A. Jones, T. Lelyveld, S. Mavrofidis, S. Kingman, N. Miles, Microwave heating applications in environmental engineering—a review, Resour Conserv Recycl 34 (2002) 75–90.

[25] F. Lin, Z. Jiang, N. Tang, C. Zhang, T. Liu, B. Dong, Photocatalytic oxidation of thiophene on $RuO_2/SO_4{}^{2-}$-TiO_2: insights for cocatalyst and solid-acid, Appl Catal B 188 (2016) 253–258.

[26] P. Bhaumik, P.L. Dhepe, Solid acid catalyzed synthesis of furans from carbohydrates, Catal Rev Sci Eng 58 (2016) 36–112.

[27] J. Liu, J. Xu, R. Che, H. Chen, M. Liu, Z. Liu, Hierarchical Fe_3O_4@ TiO_2 yolk–Shell microspheres with enhanced microwave-absorption properties, Chem Eur J 19 (2013) 6746–6752.

[28] M. Zhou, X. Zhang, J. Wei, S. Zhao, L. Wang, B. Feng, Morphology-controlled synthesis and novel microwave absorption properties of hollow urchinlike α-MnO_2 nanostructures, J Phys Chem C 115 (2010) 1398–1402.

[29] T. Xia, C. Zhang, N.A. Oyler, X. Chen, Hydrogenated TiO_2 nanocrystals: a novel microwave absorbing material, Adv Mater 25 (2013) 6905–6910.

[30] C. D'Urso, G. Bonura, A. Aricò, Synthesis and physical-chemical characterization of nanocrystalline Ta modified TiO_2 as potential support of electrocatalysts for fuel cells and electrolyzers, Int J Hydrogen Energy 42 (2017) 28011–28021.

[31] Y. Zhukova, Y. Pustov, A. Konopatsky, S. Dubinskiy, M. Filonov, V. Brailovski, Corrosion fatigue and electrochemical behavior of superelastic Ti-Nb-Ta alloy for medical implants under cyclic load conditions, Mater Today Proc 2 (2015) S991–S994.

[32] T. Moriga, R. Minakata, Y. Nomura, H. Ishikawa, K.-i. Murai, M. Mori, Stability and electrical conductivity of Nb-or Ta-doped $SrTiO_3$ perovskites for interconnectors in solid oxide fuel cells, J Ceram Soc Jpn 125 (2017) 223–226.

[33] J.-P. Niemelä, Y. Hirose, T. Hasegawa, M. Karppinen, Transition in electron scattering mechanism in atomic layer deposited Nb: TiO_2 thin films, Appl Phys Lett 106 (2015) 042101.

[34] S. Ozkan, A. Mazare, P. Schmuki, Extracting the limiting factors in photocurrent measurements on TiO_2 nanotubes and enhancing the photoelectrochemical properties by Nb doping, Electrochim Acta 176 (2015) 819–826.

[35] H.-Y. Wang, J. Chen, F.-X. Xiao, J. Zheng, B. Liu, Doping-induced structural evolution from rutile to anatase: formation of Nb-doped anatase TiO_2 nanosheets with high photocatalytic activity, J Mater Chem A 4 (2016) 6926–6932.

[36] Y. Han, C.-j. Liu, Q. Ge, Interaction of Pt clusters with the anatase TiO_2 (101) surface: a first principles study, J Phys Chem B 110 (2006) 7463–7472.

[37] B.J. Morgan, G.W. Watson, A density functional theory + U study of oxygen vacancy formation at the (110),(100),(101), and (001) surfaces of rutile TiO_2, J Phys Chem C 113 (2009) 7322–7328.

[38] M. He, X.-H. Lu, X. Feng, L. Yu, Z.-H. Yang, A simple approach to mesoporous fibrous titania from potassium dititanate, Chem Commun (2004) 2202–2203.

[39] J.L. Ropero-Vega, A. Aldana-Pérez, R. Gómez, M.E. Niño-Gómez, Sulfated titania [$TiO_2/SO_4{}^{2-}$]: a very active solid acid catalyst for the esterification of free fatty acids with ethanol, Appl Catal A Gen 379 (2010) 24–29.

[40] L.K. Noda, R.M. de Almeida, L.F.D. Probst, N.S. Gonçalves, Characterization of sulfated TiO_2 prepared by the sol–gel method and its catalytic activity in the n-hexane isomerization reaction, J Mol Catal A Chem 225 (2005) 39–46.

[41] F. Babou, G. Coudurier, J.C. Vedrine, Acidic properties of sulfated zirconia: an infrared spectroscopic study, J Catal 152 (1995) 341–349.

[42] M. Watanabe, Y. Aizawa, T. Iida, R. Nishimura, H. Inomata, Catalytic glucose and fructose conversions with TiO_2 and ZrO_2 in water at 473K: relationship between reactivity and acid–base property determined by TPD measurement, Appl Catal A Gen 295 (2005) 150–156.

[43] F. Lónyi, J. Valyon, J. Engelhardt, F. Mizukami, Characterization and catalytic properties of sulfated ZrO_2–TiO_2Mixed oxides, J Catal 160 (1996) 279–289.

[44] Q.B. Wu, Y.N. Yan, Q. Zhang, J.H. Lu, Z.J. Yang, Y.H. Zhang, Y. Tang, Catalytic dehydration of carbohydrates on InSitu exfoliatable layered niobic acid in an aqueous system under microwave irradiation, Chemsuschem 6 (2013) 820–825.

[45] C. Antonetti, M. Melloni, D. Licursi, S. Fulignati, E. Ribechini, S. Rivas, J.C. Parajo, F. Cavani, A.M.R. Galletti, Microwave-assisted dehydration of fructose and inulin to HMF catalyzed by niobium and zirconium phosphate catalysts, Appl Catal B 206 (2017) 364–377.

[46] M. Francavilla, S. Intini, L. Luchetti, R. Luque, Tunable microwave-assisted aqueous conversion of seaweed-derived agarose for the selective production of 5-hydroxymethyl furfural/levulinic acid, Green Chem 18 (2016) 5971–5977.

[47] T.S. Hansen, J.M. Woodley, A. Riisager, Efficient microwave-assisted synthesis of 5-hydroxymethylfurfural from concentrated aqueous fructose, Carbohydr Res 344 (2009) 2568–2572.

[48] S. Caratzoulas, T. Courtney, D.G. Vlachos, Hybrid quantum mechanics/molecular mechanics-based molecular dynamics simulation of acid-catalyzed dehydration of polyols in liquid water, J Phys Chem A 115 (2011) 8816–8821.

[49] R.V. Decareau, Microwaves in the Food Processing Industry, Academic Press, 1985.

[50] Y. Zhang, Y. Huang, T. Zhang, H. Chang, P. Xiao, H. Chen, Z. Huang, Y. Chen, Broadband and tunable high-performance microwave absorption of an ultralight and highly compressible graphene foam, Adv Mater 27 (2015) 2049–2053.

[51] Q. Liu, Q. Cao, H. Bi, C. Liang, K. Yuan, W. She, Y. Yang, R. Che, CoNi@ SiO_2@ TiO_2 and CoNi@ Air@ TiO_2 microspheres with strong wideband microwave absorption, Adv Mater 28 (2016) 486–490.